

Microlensing of Central Images in Strong Gravitational Lens Systems

Gregory Dobler^{1,2}, Charles R. Keeton³, & Joachim Wambsganss⁴

¹*Department of Physics and Astronomy, University of Pennsylvania, 209 S. 33rd Street, Philadelphia, PA 19104 USA*

²*Harvard-Smithsonian Center for Astrophysics, 60 Garden Street, MS-51, Cambridge, MA 02138 USA*

³*Department of Physics and Astronomy, Rutgers University, 136 Frelinghuysen Road, Piscataway, NJ 08854 USA*

⁴*Astronomisches Rechen-Institut, Zentrum für Astronomie, Universität Heidelberg, Mönchhofstrasse 12-14, 69120 Heidelberg, Germany*

5 February 2008

ABSTRACT

We study microlensing of the faint images that form close to the centers of strong gravitational lens galaxies. These central images, which have finally begun to yield to observations, naturally appear in dense stellar fields and may be particularly sensitive to fine granularity in the mass distribution. The microlensing magnification maps for overfocussed (i.e., demagnified) images differ strikingly from those for magnified images. In particular, the familiar “fold” and “cusp” features of maps for magnified images are only present for certain values of the fraction f of the surface mass density contained in stars. For *central* images, the dispersion in microlensing magnifications is generally larger than for normal (minimum and saddle) images, especially when the source is comparable to or larger than the stellar Einstein radius. The dispersion depends in a complicated way on f ; this behaviour may hold the key to using microlensing as a probe of the relative densities of stars and dark matter in the cores of distant galaxies. Quantitatively, we predict that the central image C in PMN J1632–0033 has a magnification dispersion of 0.6 magnitudes for $R_{\text{src}}/R_E \lesssim 1$, or 0.3 mag for $R_{\text{src}}/R_E = 10$. For comparison, the dispersions are 0.5–0.6 mag for image B and 0.05–0.1 mag for image A, if $R_{\text{src}}/R_E \lesssim 1$; and just 0.1 mag for B and 0.008 mag for A if $R_{\text{src}}/R_E = 10$. (The dispersions can be extrapolated to larger source sizes as $\sigma \propto R_{\text{src}}^{-1}$.) Thus, central images are more susceptible than other lensed images to microlensing and hence good probes for measuring source sizes.

Key words: galaxies — stellar populations — gravitational lensing

1 INTRODUCTION

Two aspects of strong gravitational lensing that date back 25 years have attracted much recent interest. Microlensing, or variations in the (optical and/or x-ray) fluxes of lensed quasar images that are induced by individual stars in the lens galaxy, was first discussed by Chang & Refsdal (1979). The phenomenon has now been observed in several lens systems (Woźniak et al. 2000; Schechter et al. 2003; Richards et al. 2004; Gaynullina et al. 2005; Kochanek et al. 2006; Morgan et al. 2006). It can be used to learn about the stellar components (Gott 1981; Wambsganss et al. 1990b; Pelt et al. 1998; Schmidt & Wambsganss 1998; Wyithe et al. 2000; Kochanek 2004) and the relative densities of stars and dark matter (Schechter & Wambsganss 2002, 2004) in lens galaxies, and to probe structure in the source quasars at stunning micro-arcsecond resolution (Grieger et al. 1988, 1991; Agol & Krolik 1999;

Mineshige & Yonehara 1999; Fluke & Webster 1999; Richards et al. 2004; Goicoechea et al. 2004).

Central or “odd” lensed images were originally predicted by Dyer & Roeder (1980) and Burke (1981). If the inner surface mass density of a lens galaxy is shallower than $\Sigma \propto R^{-1}$ and there is no point mass at the center, then lensing should always produce an odd number of images. Nearly all observed lenses, however, exhibit two or four images. The prediction and observations can be reconciled by noting that one of the expected images should be very close to the center of the lens galaxy and demagnified by the high central surface density there (e.g., Wallington & Narayan 1993; Norbury et al. 2000; Rusin & Ma 2001; Keeton 2003). That makes central images difficult to detect — and indeed the first ones have only just been found. Winn et al. (2003, 2004) detected a central image at radio wavelengths in the asymmetric 2-image lens PMN J1632–0033, while Inada et al. (2005) detected a central image at optical wavelengths in the unusual 4-image cluster lens SDSS J1004+4112.

Image	κ	γ	μ
A	0.370	0.422	4.570
B	3.309	2.859	0.352
C	16.517	13.796	0.020

Table 1. Total convergence κ , shear γ , and magnification μ for each of the three images in PMN J1632–0033, from spherical power law plus external shear lens models by Winn et al. (2003, 2004). “C” indicates the central, highly demagnified image.

Our goal in this paper is to combine the two phenomena and study microlensing of central images. The issue is timely since central images are now being observed, and compelling since the images naturally form in regions where the density of stars is high and microlensing seems inevitable.

We customize our calculations to the lens PMN J1632–0033, because it is both a known central image system and also a prototype for the sorts of systems that are expected to yield the most central images in the future (Keeton 2003; Bowman et al. 2004). Winn et al. (2003, 2004) recently studied a wide range of mass models for PMN J1632–0033, which can be used to estimate the total convergence κ and shear γ at the positions of the images. The lens data, including the central image, are consistent with a simple power law surface mass density $\Sigma \propto R^{-\alpha}$ with $\alpha = 0.91 \pm 0.02$, plus a small external tidal shear. Table 1 gives the values of κ and γ for such a model, which we adopt as inputs for our microlensing simulations.

2 METHODS

We use standard methods for microlensing calculations (Wambsganss 1999). Specifically, we pick a patch around an image that is large compared with a stellar Einstein radius (the scale for microlensing), but small compared with the global scale of the lens so that the mean densities of stars and dark matter are essentially constant across the patch. Attaining this balance is not difficult because the global scale is set by the $1''.5$ image separation while the stellar Einstein radius is $R_E \sim 2 (M/M_\odot)^{1/2} \times 10^{-6}$ arcsec. In practice, we typically consider a rectangular patch in the image plane chosen so that it maps into a square patch in the source plane that is $100R_E$ on a side (see below). Without loss of generality, we can choose a coordinate system aligned with the direction of the local shear. We assume that a fraction

$$f = \kappa_{\text{stars}} / \kappa_{\text{tot}} \quad (1)$$

of the total surface mass density (or convergence) is contributed by stars. We use that to determine the number density of stars in the image plane patch,

$$n_* = \frac{f \kappa_{\text{tot}}}{\pi R_E^2}, \quad (2)$$

and then distribute the stars randomly. The total surface density κ_{tot} is kept fixed (to the values in Table 1) by including a smooth, continuous matter component with $\kappa_c = (1 - f)\kappa_{\text{tot}}$. Paczynski (1986) has shown that including a smooth matter component is equivalent to rescaling the convergence and shear to

$$(\kappa^{\text{eff}}, \gamma^{\text{eff}}) = \frac{(\kappa, \gamma)}{|1 - \kappa_c|}, \quad (3)$$

with $f = 100\%$ in stars. For the case of a finite source, this also leads to a rescaling of the source size,

$$R_{\text{src}}^{\text{eff}} = \frac{R_{\text{src}}}{|1 - \kappa_c|}. \quad (4)$$

In this pilot study, we assume that all stars have the same mass, and we always work in units of the stellar Einstein radius R_E . Previous analyses have shown that the microlensing magnification distribution is at best weakly dependent on the distribution of stellar masses, at least for a point source.¹ That result must break down for a finite source, which would be insensitive to stars below some mass threshold (roughly corresponding to $R_E \lesssim R_{\text{src}}$). The full problem — microlensing of a finite source by stars with unequal masses — is certainly interesting, but beyond the scope of this paper (cf. Congdon et al. 2006).

We use ray-shooting software by Wambsganss (1990), Wambsganss et al. (1990b), and Wambsganss (1999) to perform the microlensing simulations. Briefly, the software “shoots” a large number ($\gtrsim 10^8$) of light rays from the observer through the lens/image plane into the source plane, and collects them in small pixels. The number of rays in a source pixel is proportional to the lensing magnification at that position. As described by Wambsganss (1999), the rectangular shooting patch in the image plane is larger than the region that would map into the source plane box in the absence of microlensing. The reason is that the deflection diverges as $1/r$ near a star, so stars outside the nominal shooting region can send light rays into the source plane box (Katz et al. 1986). The shooting region is expanded to ensure that a significant fraction of this “diffuse flux” is collected.

The ray-shooting software produces a magnification map in the source plane. We can obtain the magnification probability distribution by making a histogram of the pixel magnifications. To consider a source with a finite extent, we convolve the magnification map with the surface brightness distribution of the source before making the histogram. For simplicity, we use a Gaussian source with half-light radius R_{src} , since Mortonson et al. (2005) argue that the detailed structure of the source hardly affects magnification distributions provided that the half-light radius is the same (also see Congdon et al. 2006).

The physical input parameters for the simulations are the total convergence and shear, which we take from Table 1, and the fraction f of mass in stars, which we vary (see §3). The technical input parameters are the size of the magnification map and the number of pixels. We seek to consider sources both smaller and larger than R_E , and in particular find the range $0.1 \leq R_{\text{src}}/R_E \leq 10$ to be both interesting and tractable. In order to have many independent source positions in a given magnification map, we use maps that are $100R_E$ on a side. In order to have enough pixels to handle small sources, we use maps with 1024×1024 pixels.

¹ The magnification distribution was long thought to be independent of the microlens mass function (Schneider 1987; Wambsganss 1992; Lewis & Irwin 1995; Wyithe & Turner 2001). However, Schechter et al. (2004) recently presented results from numerical experiments suggesting that there is a weak dependence.

To obtain fair sampling, we create 50 independent magnification maps for each image, and compute the final magnification distributions from the combination of all of them. A fringe benefit of this approach is that we can consider the 50 magnification maps to be independent realizations of the microlensing calculation, and use bootstrap or jackknife resampling (e.g., Efron 1982) to estimate the statistical uncertainties in our analysis.

3 RESULTS

3.1 Magnification maps

Figure 1 shows magnification maps for $f = 100\%$ of the surface density in stars. To display the range of features that appear on different length scales, we show $(100R_E)^2$, $(30R_E)^2$, and $(10R_E)^2$ maps here. The maps for image C in particular show that there is structure on scales of tens of Einstein radii, so even a $(100R_E)^2$ map does not contain a fully representative sample of magnifications.

The qualitative differences in the three magnification maps shown in Figure 1 are striking. For image A, which forms at a local minimum in the time delay surface and has relatively low values of the convergence and shear leading to a modest amplification, the map shows the familiar caustic network (e.g., Wambsganss 1990; Schneider et al. 1992; Wambsganss 1999). The caustics are preferentially stretched along the horizontal axis because we have chosen coordinates aligned with the local shear. For image B, which forms at a saddle point in the time delay surface and is modestly demagnified, careful inspection reveals that the map shows many of the 3-pointed cusps that are characteristic of microlensing when the parity is negative (e.g., Schneider et al. 1992; Petters et al. 2001). These results are familiar. More surprising is the map for image C, which forms at a local maximum in the time delay surface and is highly demagnified. This map looks very different from the familiar, traditional caustics. It exhibits round, concentrated blobs of high magnification, surrounded by large regions of low magnification. These features are known to occur for highly overfocussed (i.e., demagnified) microlensing scenarios (e.g., Wambsganss 1990; Schneider et al. 1992; Petters & Witt 1996; Petters et al. 2001), but they have not been explored in great detail.²

As noted above, there appears to be strong inhomogeneity even on scales of tens of Einstein radii. To quantify this, we define the auto-correlation function along linear slices through the maps (see Wambsganss et al. 1990a):

$$\xi(\Delta x) = \frac{\langle \mu(x)\mu(x + \Delta x) \rangle - \langle \mu(x) \rangle^2}{\langle \mu(x)^2 \rangle - \langle \mu(x) \rangle^2}, \quad (5)$$

where $\mu(x)$ is the magnification at position x and the averages are over all positions along the slice. For each map, we calculate $\xi(\Delta x)$ for each row and average over rows. We then further average over 50 maps (i.e., 50 random stellar configurations). This gives $\xi(\Delta x)$ parallel to the shear axis; we then

repeat the procedure averaging over columns to find $\xi(\Delta x)$ perpendicular to the shear. The auto-correlation function for each image, both parallel and perpendicular to the shear, is shown in Figure 2. The distance Δx_0 at which $\xi(\Delta x)$ falls to zero is a measure of the correlation length.

Parallel to the shear, $\Delta x_0^B \approx 6.1R_E$ while $\Delta x_0^C \approx 10.6R_E$, implying that the image B maps have structures spanning ~ 10 – $15 R_E$ and the image C maps have structures ~ 20 – $25 R_E$. It is difficult to interpret ξ^A parallel to the shear since the caustics are preferentially stretched along the shear axis, leading to substantial power in ξ^A even at large Δx . Perpendicular to the shear, ξ^A falls rapidly to zero ($\Delta x_0^A \approx 2.3R_E$ along this direction) and in fact Figure 1 shows little in the way of large scale structure in the vertical direction. For images C and B, we see that $\xi^C > \xi^B$ for all distances Δx . This supports the qualitative conclusion that there is more structure on large scales for the image C compared to image B maps.

So far we have assumed that $f = 100\%$ of the surface mass density for each image is in stars, which is probably valid for image C but unlikely for image A. In Figures 3–5 we examine the magnification maps for different values of f . In Figure 3, when f is low, the map exhibits caustics of individual stars, and as f increases the number of caustics increases and they begin to merge (cf. Schechter & Wambsganss 2002).

Figures 4 and 5 show drastically different behaviour. For image C (Figure 5), the caustics morph from blobs to cusps as f decreases; by $f = 0.2$ the magnification map consists entirely of fold and cusp caustics. Decreasing f further causes holes to appear in the magnification map (Chang & Refsdal 1984). For image B, we find the curious result that cusp caustics are present for $f = 1.0$ (Figure 1), but they are absent for $0.9 \gtrsim f \gtrsim 0.5$, and then they reappear at lower f values. This behaviour is surprising because it was not seen by Schechter & Wambsganss (2002) in their magnification maps for a highly magnified saddle image. Since our image B is a demagnified saddle image, we conjecture that the overall magnification, in addition to the parity, is important for determining whether the caustics are blobs or cusps and folds. The dependence on the stellar mass fraction appears to be complicated.

3.2 Magnification distributions

The magnification distributions for different source sizes and different images are shown in Figure 6 (assuming $f = 100\%$). The magnification is expressed as the change in magnitude due to the presence of microlensing, $\Delta m = -2.5 \log(\mu/\mu_0)$. In general, the distributions appear to be smooth and fairly symmetric about $\Delta m = 0$. The exception is the case of image A with a small source ($R_{\text{src}}/R_E \lesssim 0.1$), whose magnification distribution shows three distinct peaks. The peaks can be understood in terms of the caustic network (e.g., Rauch et al. 1992; Wambsganss et al. 1992; Granot et al. 2003): from high to low Δm — i.e., low to high μ —, the first peak corresponds to sources outside all caustics, the second peak to sources inside a single caustic (so there is one additional pair of microimages), and the third peak to sources inside a pair of overlapping caustics (so there are two extra microimage pairs). In fact, there are higher-order peaks corresponding to source positions where more caustics

² Petters & Witt (1996) and Petters et al. (2001, see Chapter 15) have shown that, in the case of an isolated star with a constant shear and a large, constant convergence κ_c , the caustics consist entirely of elliptical fold curves and do not have any cusps.

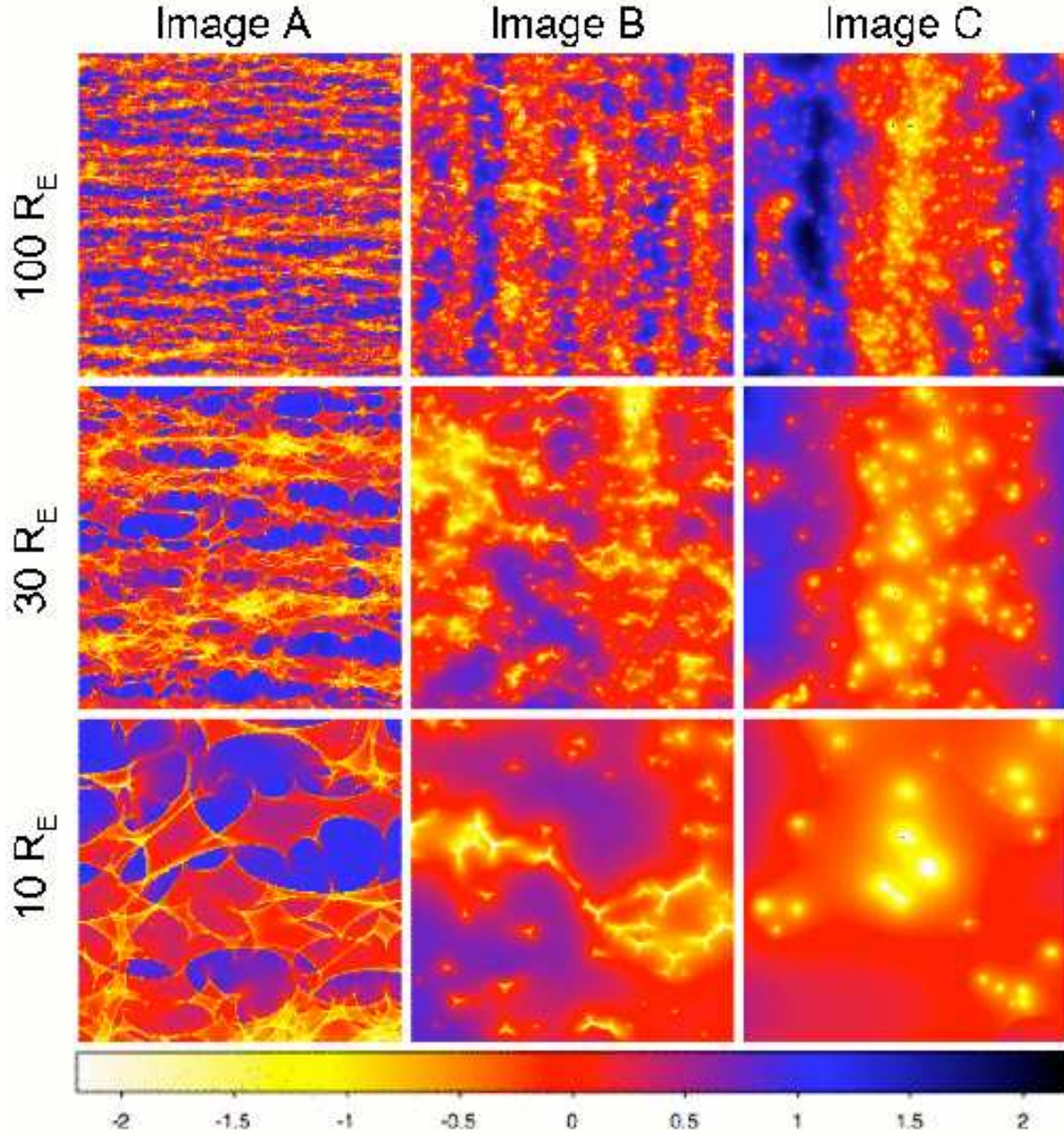


Figure 1. Sample magnification maps for images A (left), B (center), and C (right). The top row shows $100R_E$ on a side, the middle row shows $30R_E$ on a side, and the bottom row shows $10R_E$ on a side. The zoom in region in each case is centered on the $(100R_E)^2$ map. The fraction of surface mass density in stars is $f = 100\%$ for all cases, and the colorbar at the bottom indicates the change in magnitude, with respect to the mean magnification, at each source position (yellow regions indicate magnification, blue regions indicate demagnification).

overlap, but those peaks blur together and do not appear as clear features in the final magnification distribution (see Granot et al. 2003, especially their Fig. 4). The multi-peak structure disappears as the source size increases, because a large source ($R_{\text{src}}/R_E \gtrsim 1$) generally extends over one or more caustics, so the regions of different image multiplicity in the source plane are smeared out and disappear as distinct maxima in the magnification distribution. The multi-peak structure is not apparent in the histograms for images B and C, even for sources as small as $R_{\text{src}} = 0.1R_E$, because

the caustics are so small that only a small fraction of source positions lead to additional microimage pairs.

An important qualitative feature of the magnification distributions is that the width decreases as the source size increases. The width can be considered to represent either the likelihood that the magnification at any given time is different from what a smooth model would predict, or the RMS amplitude of variations in time. Thus, we may say that the larger the source, the less it is affected by microlensing — a well known result which makes intuitive sense. To quantify this effect, we compute the dispersion in magnitudes, namely

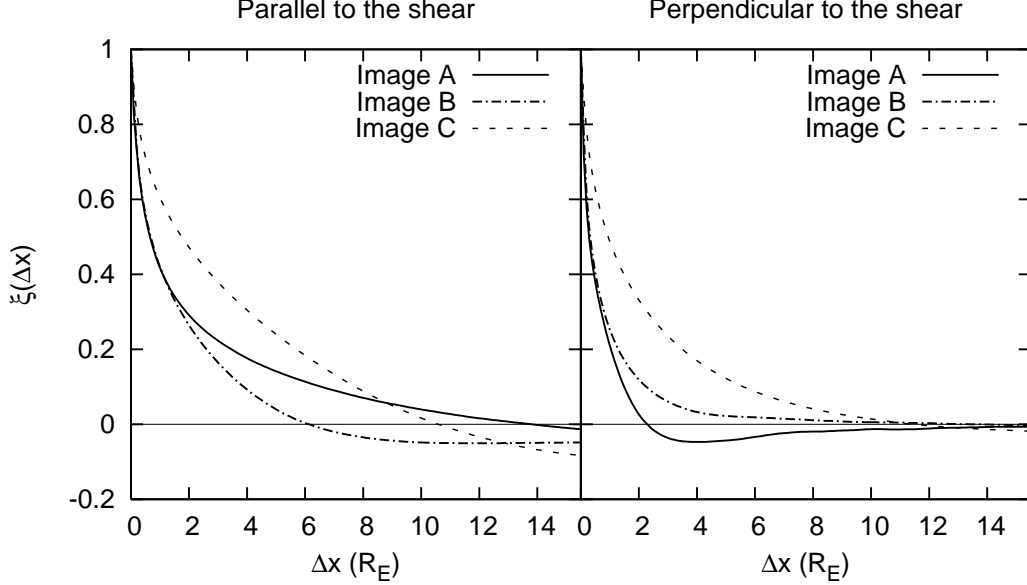


Figure 2. One-dimensional auto-correlation functions for magnification maps with $f = 100\%$. The left panel shows $\xi(\Delta x)$ aligned with the shear axis, while the right panel shows $\xi(\Delta x)$ perpendicular to the shear axis. In the left panel, there is significant power in ξ^A because the caustics tend to be stretched along the shear axis. The fact that $\xi^C > \xi^B$ implies that there is structure in the image C maps on larger length scales compared to the image B maps.

$$\sigma = \left[\langle (-2.5 \log \mu)^2 \rangle - \langle -2.5 \log \mu \rangle^2 \right]^{1/2}, \quad (6)$$

where the average is over source positions. In previous work the magnification dispersion has been studied analytically (for the case of $\gamma = 0$, $\kappa_c \lesssim 1$, and $R_{\text{src}} \gtrsim 5R_E$; Refsdal & Stabell 1991; Seitz et al. 1994; Neindorf 2003), numerically (Deguchi & Watson 1987; Refsdal & Stabell 1991; Seitz et al. 1994; Refsdal & Stabell 1997; Wyithe & Turner 2002), and with ray-shooting methods (Schechter & Wambsganss 2002; Wyithe & Turner 2002; Lewis & Ibata 2004; Schechter et al. 2004; Mortonson et al. 2005).

Figure 7 shows that the dispersion falls monotonically as the source size increases (as seen in the previous work). It remains relatively constant until the source size becomes comparable to the stellar Einstein radius, and then drops rapidly. Curiously, all three images have roughly the same magnification dispersion when the source is small ($R_{\text{src}}/R_E \lesssim 0.3$). For $R_{\text{src}}/R_E \gtrsim 0.3$, the ordering of the images is independent of source size: image C is most affected by microlensing, followed by image B, and finally image A. For large sources analytic arguments suggest that the dispersion should scale as $\sigma \propto R_{\text{src}}^{-1}$ (Refsdal & Stabell 1991, 1997). We certainly see this for image A. It appears that images B and C are approaching the asymptotic scaling but have not quite reached it at $R_{\text{src}}/R_E = 10$. This is not surprising because the predicted scaling applies when the number of stars in front of the image is large. Since images B and C are demagnified, the source needs to be larger (compared with the magnified image A) in order for the image to be large enough to intercept a significant number of stars.

The next step is to consider how the magnification

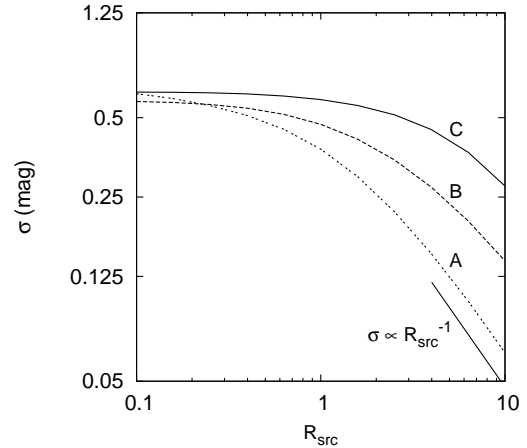


Figure 7. Magnification dispersion as a function of source size, for the three images, assuming $f = 100\%$ of the mass in stars. The line segment below the curve for image A shows the expected asymptotic scaling for large sources, $\sigma \propto R_{\text{src}}^{-1}$ (Refsdal & Stabell 1991, 1997).

dispersion changes as we decrease f , as shown in Figure 8. For images A and B, the dispersion falls monotonically as f decreases. For image B, this is in contrast to Schechter & Wambsganss (2002) who found that decreasing f can *increase* the magnification dispersion for saddle images. We believe the difference is explained by the fact

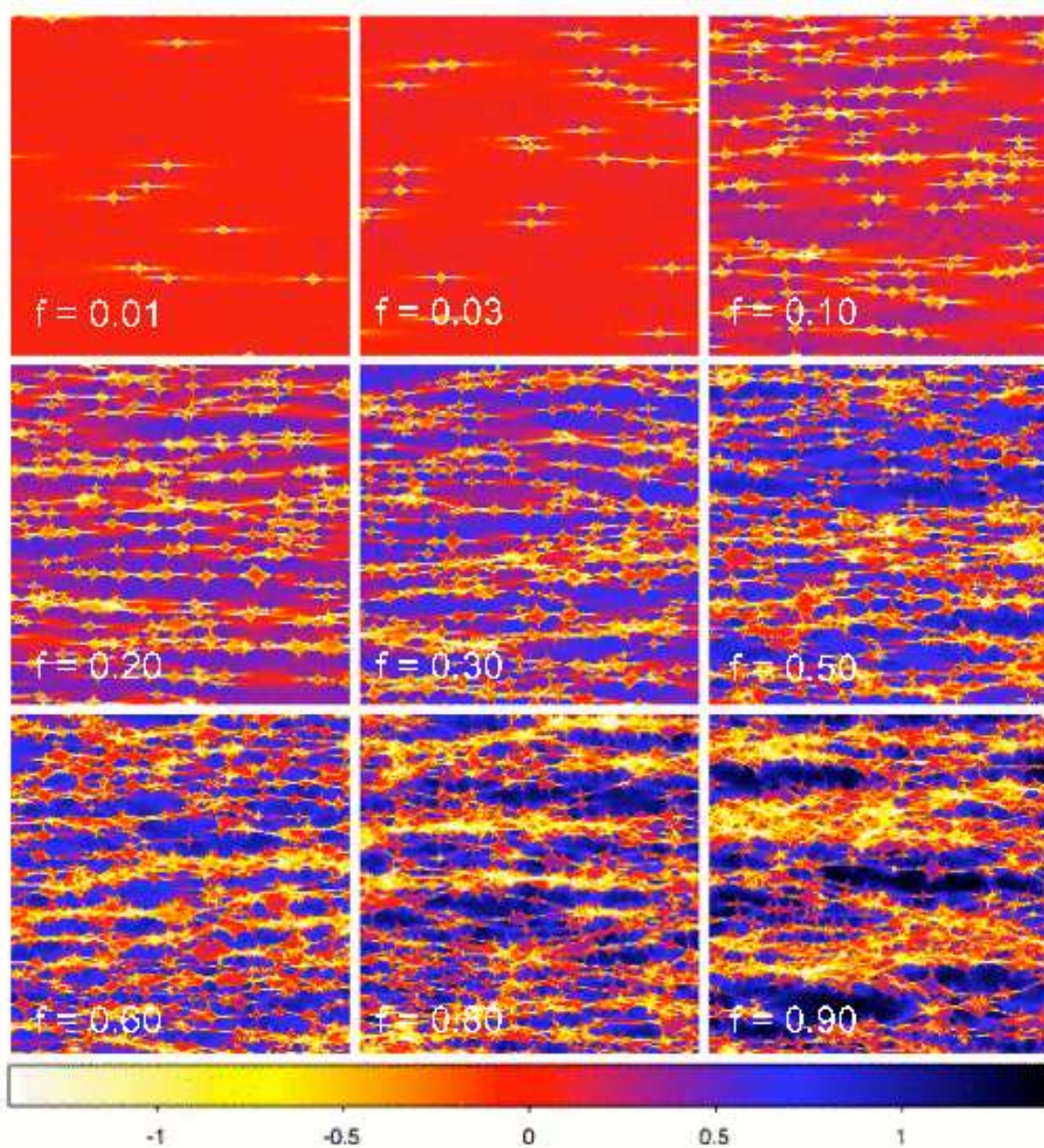


Figure 3. Magnification maps for image A with size $(50R_E)^2$ and varying f (cf. Figure 1, left column, for $f = 1.0$) The visual contrast in each map conveys the magnification dispersion. The dispersion increases with increasing f : rapidly for small f , more slowly above $f \gtrsim 0.3$ (compare to Figure 8 with $R_{\text{src}} = 0.1$).

that Schechter & Wambsganss considered a highly magnified saddle image ($\mu = 9.5$), such as would be seen in a bright minimum/saddle pair straddling a critical curve in a 4-image lens; whereas our saddle image B has a modest demagnification ($\mu = 0.35$), as is common for the image nearer the lens galaxy in an asymmetric 2-image lens.

For the central image C, we find that decreasing the fractional surface density in stars can *increase* the magnification dispersion, so long as $R_{\text{src}} \lesssim R_E$. Specifically, for a large source $R_{\text{src}}/R_E = 10$ (right panel of Figure 8), the magnification dispersion for image C decreases monotonically as f decreases, like it does for images A and B. When

$R_{\text{src}}/R_E = 1$, however, the dispersion increases as f decreases all the way down to $f \approx 0.04$, and only then turns over. (The turnover is reassuring, because for $f \rightarrow 0$ there is no microlensing and the magnification dispersion must vanish.) When $R_{\text{src}}/R_E = 0.1$, the turnover occurs at $f < 0.01$. While the behaviour of image C at low f may have little practical importance, it is still useful for understanding how the magnification dispersion depends on the relative densities of stars and dark matter.

We note that, in the limit of an infinitesimal source, the dispersion is visually apparent in the contrast of the magnification maps shown in Figures 3, 4, and 5. The dispersion in

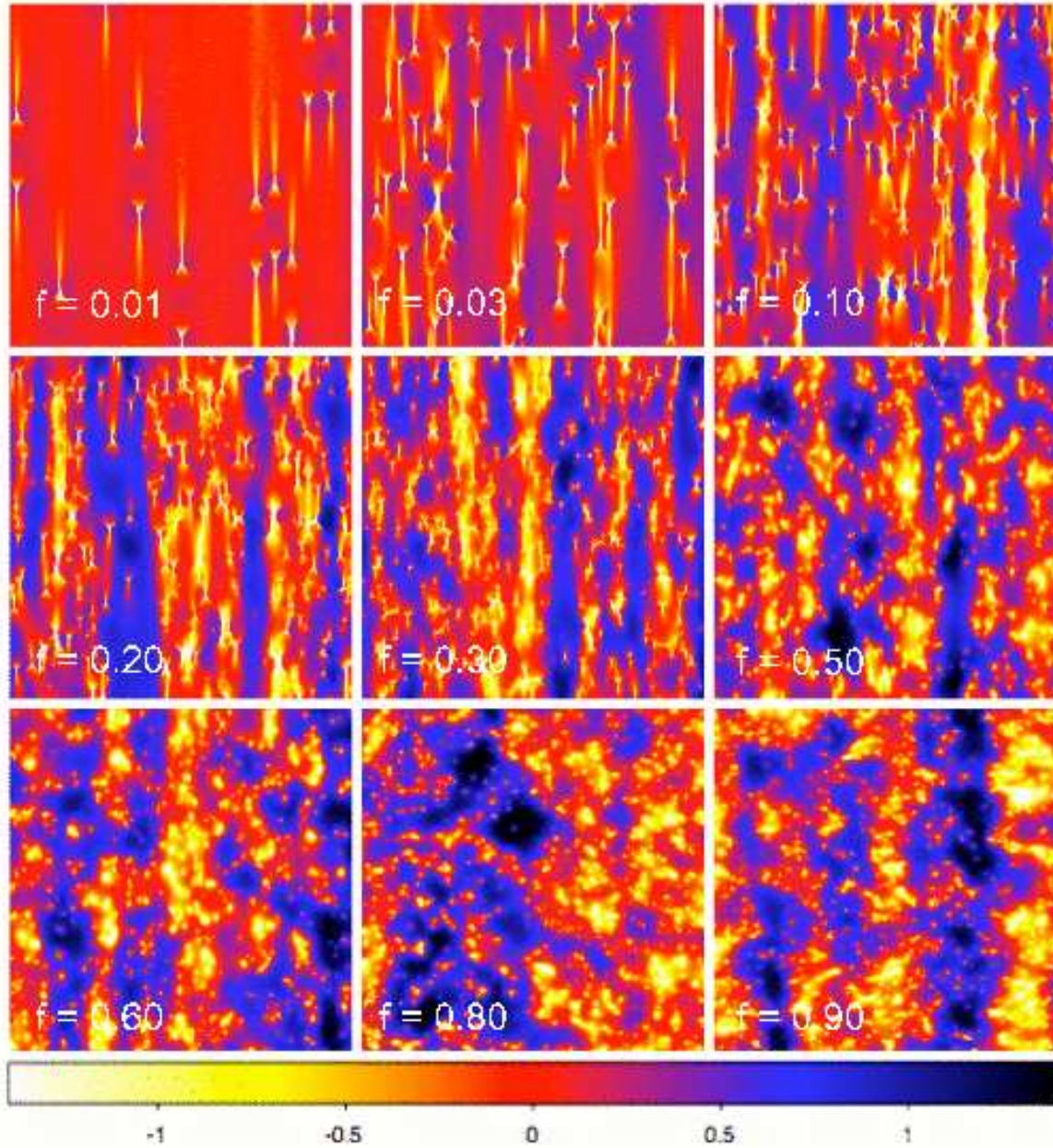


Figure 4. The same as Figure 3, but for image B (cf. Figure 1, middle column, for $f = 1.0$). The relative number of cusps and folds versus blob caustics has a complicated dependence on f . The visual contrast in each map conveys the magnification dispersion. The dispersion increases with increasing f : rapidly for small f , more slowly above $f \gtrsim 0.3$ (compare to Figure 8 with $R_{\text{src}} = 0.1$).

the maps of images A and B visibly increases with f , while the dispersion of the image C maps *decreases* with increasing f . Further, the contrast changes sharply at low f for all three images and then remains roughly constant for $f \gtrsim 0.4$. This is consistent with the slopes of the σ versus f curves shown in Figure 8.

To make a final interpretation of Figure 8, it is useful to estimate an upper bound on the fractional surface density in stars at the position of each image. For PMN J1632–0033, Winn et al. (2003) show that the lens data are consistent with a total surface mass density of the form $\kappa_{\text{tot}} \propto R^{-\alpha}$ with $\alpha = 0.91 \pm 0.02$. They note that the lens galaxy is too

faint to be characterized in detail with existing HST images, but appears to be an early-type galaxy with effective radius of $R_e \approx 0''.2$. To estimate the maximum possible stellar mass density as a function of radius, we model κ_{stars} using a de Vaucouleurs $R^{1/4}$ law profile, and set the stellar mass-to-light ratio to the largest allowed value such that κ_{stars} never exceeds κ_{tot} . Using the observed distances to the center of the lens ($R_A = 1''.38$, $R_B = 0''.09$, and $R_C = 0''.01$; see Winn et al. 2003), we obtain the f_{max} values listed in Table 2.

This analysis confirms our guess that the matter at image C could be essentially all stars. By contrast, the galaxy

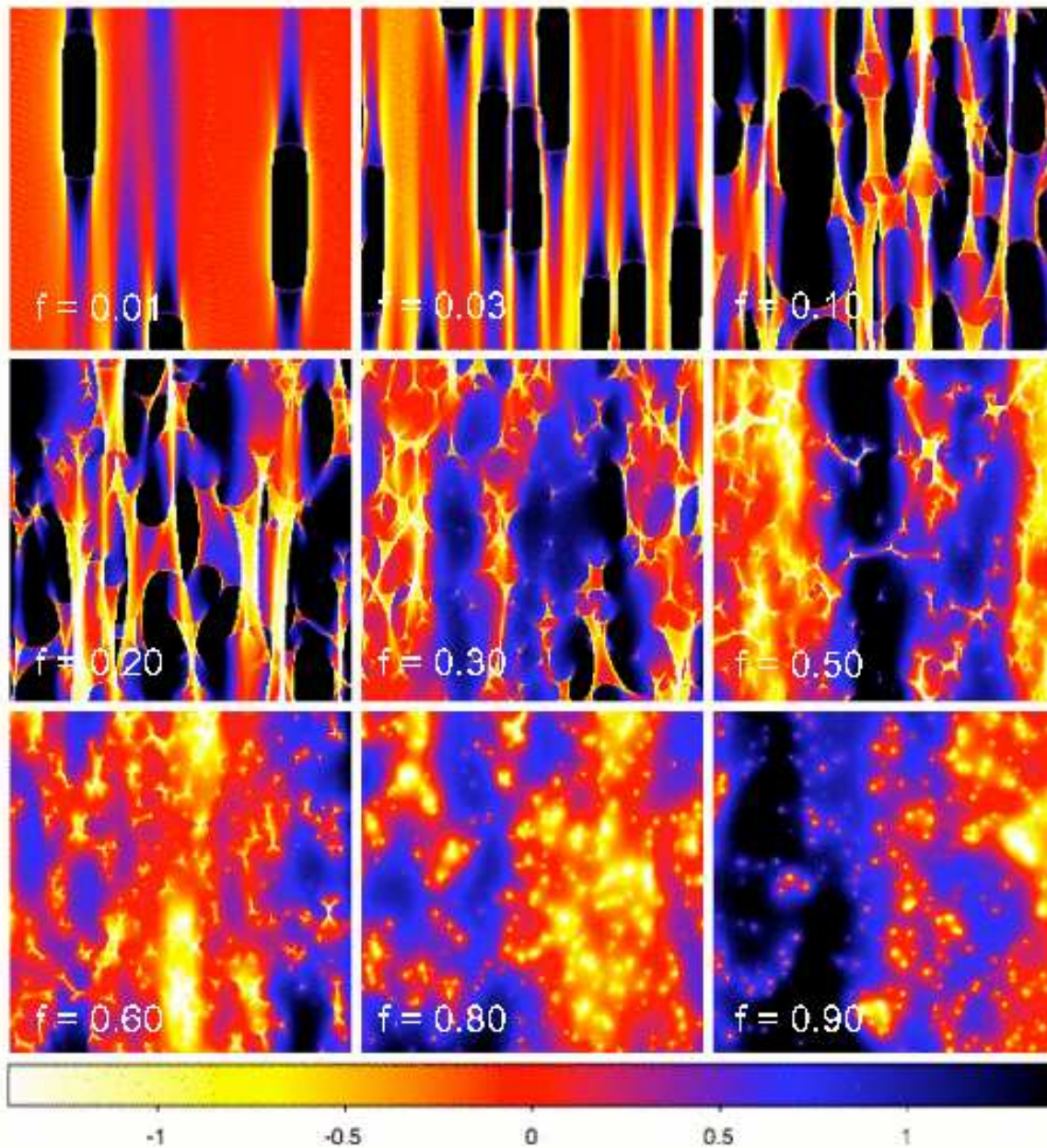


Figure 5. The same as Figure 3, but for image C (cf. Figure 1, right column, for $f = 1.0$). The relative number of cusps and folds versus blob caustics has a complicated dependence on f . The visual contrast in each map conveys the magnification dispersion. In contrast to Figures 3 and 4, the dispersion *decreases* with f , rapidly at first and then more slowly above $f \gtrsim 0.4$ (compare to Figure 8 with $R_{\text{src}} = 0.1$).

appears to be concentrated enough that at image B the density is no more than half stars, and at the distance corresponding to image A the density is no more than 1% stars. When we combine the upper limits on f with the σ versus f curves in Figure 8, we obtain the upper bounds on the magnification dispersion listed in Table 2.

The bottom line is that microlensing is basically negligible for image A, but reasonably important for both images B and C. For large source sizes, the central image C is notably more affected by microlensing than the saddle image

B, hence microlensing of such demagnified images can help reveal the source size.

4 DISCUSSION

Central lensed images, which are highly demagnified and naturally appear in places where the density of stars is high, are more susceptible to gravitational microlensing than the more familiar images that form at larger distances from lens galaxies. Therefore, it is useful to understand microlensing of central images in detail.

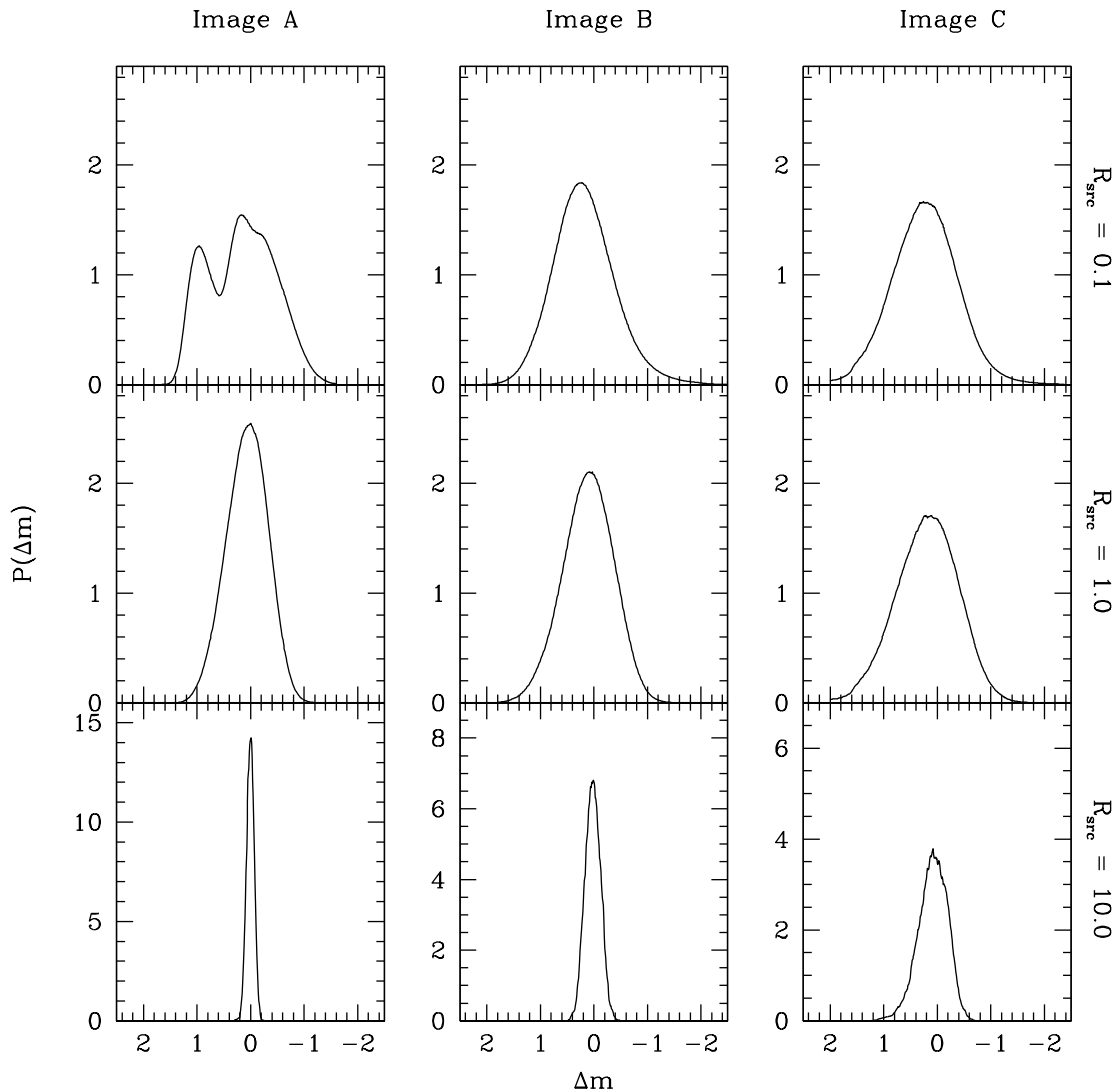


Figure 6. Magnification distributions for the three images (left to right), for three different source sizes (top to bottom), assuming $f = 100\%$ of the mass in stars. The source is modeled as a Gaussian with half-light radius R_{src} (quoted in units of R_E). The distributions for each image are derived from 50 independent realizations of $(100R_E)^2$ magnification maps. Each probability distribution $P(\log \mu)$ is normalized to unit area, but the vertical axis scale varies in the bottom panels. Any apparent jaggedness is numerical noise. The double peak in the panel at the top left is real and reflects the first additional microimage pair (for details see text). The histograms are centered on $\Delta m = -2.5 \log(\mu/\mu_0) = 0$, where μ_0 is the magnification in the absence of microlensing (from Table 1.) The microlensing distributions yield a mean magnification $\langle \mu \rangle$ that agrees with μ_0 to within numerical uncertainties.

The microlensing magnification maps for demagnified images differ qualitatively from those for familiar magnified images in striking ways. For high fractional surface density in stars, the central image maps do not show any of the classic fold and cusp caustic structures, but rather have concentrated blobs of high magnification amid large regions of demagnification. As f is decreased the maps begin to develop more and more cusps and folds. For the demagnified saddle, low values of f yield cusps and folds, intermediate values produce blobs, and at very large values ($f \approx 100\%$) the cusps and folds reappear. Thus the relative number of cusps and folds versus blobs has a complicated dependence on κ_{tot} , γ , and f (see also Petters et al. 2001).

The central image C maps also show notable inhomogeneity on scales of tens of Einstein radii. These large scale structures are evident in the 1-D auto-correlation function $\xi(\Delta x)$. For the central image C, ξ^C falls to zero by $\Delta x_0^C \approx 10.6R_E$ along the direction parallel to the shear, implying structure sizes $\sim 20\text{--}25R_E$. In contrast $\Delta x_0^B \approx 6.1$ suggesting smaller structures with sizes $\sim 10\text{--}15R_E$. The larger scale structures in the image C maps causes microlensing fluctuations to be larger for demagnified central images than for other images, even when the source is fairly large ($R_{\text{src}}/R_E \gtrsim 1$).

Our most intriguing qualitative result concerns the sensitivity of central image microlensing to the relative

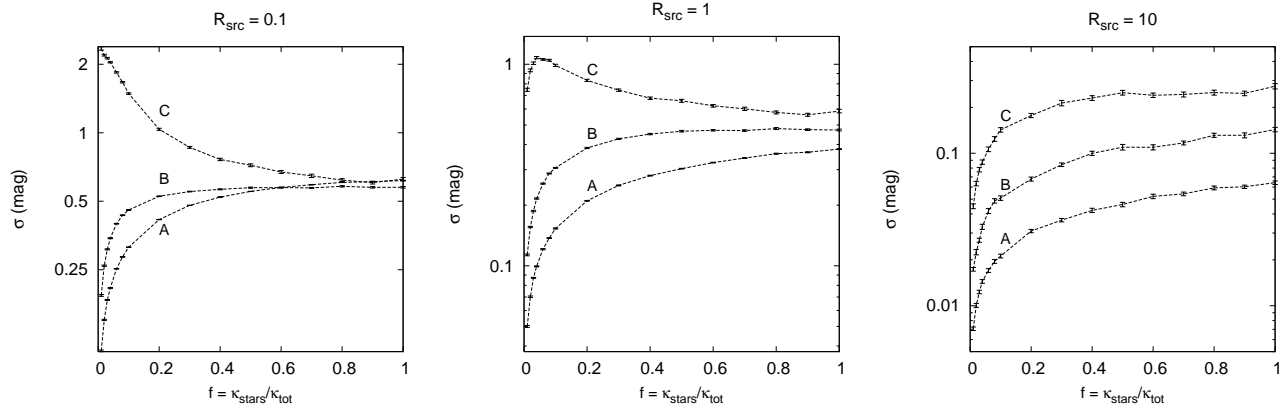


Figure 8. Magnification dispersion as a function of the fractional surface density in stars, $f = \kappa_{\text{stars}}/\kappa_{\text{tot}}$, for three different source sizes (quoted in units of R_E). The three lines show the three images A (bottom), B (middle), and C (top) of PMN J1632–0033. Note the widely different scales for σ . The errorbars indicate the statistical uncertainties estimated with bootstrap and jackknife resampling (e.g., Efron 1982).

Image	f_{max}	σ (in mag)		
		$R_{\text{src}} = 0.1$	1	10
A	0.013 ± 0.001	0.13	0.05	0.008
B	0.511 ± 0.023	0.58	0.48	0.10
C	0.997 ± 0.003	0.63	0.58	0.28

Table 2. Column 2 gives our estimate of the upper limit on $f = \kappa_{\text{stars}}/\kappa_{\text{tot}}$ (see text). The quoted uncertainties are derived from the uncertainty in the power law index of the lens galaxy mass distribution ($\alpha = 0.91 \pm 0.02$; Winn et al. 2003). Columns 3–5 give upper limits on the magnification dispersion σ (in magnitudes), for three source sizes (quoted in units of R_E). These upper limits were obtained by combining f_{max} with the σ vs. f curves in Figure 8. The uncertainties in σ due to the uncertainties in f_{max} are $\ll 0.13$ mag. The dispersion can be extrapolated to larger source sizes with the scaling $\sigma \propto R_{\text{src}}^{-1}$ (Refsdal & Stabell 1991, 1997).

densities of stars and dark matter. When the source is large ($R_{\text{src}}/R_E \gtrsim 3$), the magnification dispersion decreases monotonically with the fraction f of density in stars. However, when the source is small ($R_{\text{src}}/R_E \lesssim 3$), the magnification dispersion *rises* as f is decreased from unity, reaches a peak at some finite value of f , and then falls to zero as $f \rightarrow 0$ (as it should in the absence of microlensing). This dependence is similar to the behaviour seen by Schechter & Wambsganss (2002) for a highly magnified saddle image. We do not see such behaviour for a demagnified saddle, but we do see it for a demagnified central image. While this qualitative result has little practical importance (we expect $f \approx 1$ for central images), it may be valuable as insight into how microlensing depends on the relative amounts of stars and dark matter. If we can develop a full understanding of that problem, we may be able to turn microlensing into the best tool available for probing local *densities*, rather than integrated masses, of dark matter in distant galaxies (see Schechter & Wambsganss 2002, 2004).

One practical goal of microlensing studies is to probe the structure of the optical continuum emission regions of quasars at very high effective spatial resolution. The

light curves produced by relative motion of the lens galaxy and source quasar can be used to map out the (1-dimensional) structure of the quasar on micro-arcsecond scales (Grieger et al. 1988, 1991; Agol & Krolik 1999; Mineshige & Yonehara 1999; Fluke & Webster 1999; Goicoechea et al. 2004). In terms of raw variability amplitude, it would seem that central images are the best targets for microlensing observations. Of course, there is the problem of detecting central images at optical wavelengths in the first place. A faint central image may be swamped by light from the lens galaxy. It may also be dimmed by extinction or scattering in the interstellar medium of the lens galaxy, although those effects might not be too much of a concern in the vast majority of lens galaxies that are ellipticals.

It is interesting to consider the possibility that central image microlensing may allow us to probe the size of the *radio* emission region of the source quasar. For large sources the dispersion scales as $\sigma \propto R_{\text{src}}^{-1}$, so for radio sources with $R_{\text{src}}/R_E \gtrsim 100$ we expect microlensing fluctuations to be no more than a few percent.³ For the case of PMN J1632–0033, the intensity of the central image is ~ 750 and $500 \mu\text{Jy}$ at 8 and 22 GHz, respectively (Winn et al. 2004), so microlensing fluctuations may be at the level of tens of μJy . Presently, integration times for observing these fluctuations are prohibitively long for a monitoring campaign (~ 5 or 50 hrs at 8 or 22 GHz to resolve 5% fluctuations)⁴. However, next generation telescopes such as the EVLA or EMERLIN will make these observations feasible.

Our results allow us to consider how microlensing may affect various other applications that involve central lensed images. In PMN J1632–0033, the position and brightness of the central image lead to strong constraints on the density profile of the lens galaxy, and to upper limits on the

³ However, Koopmans & de Bruyn (2000) report that there is evidence for microlensing fluctuations in at least one radio lens, B1600+434. Additionally, scintillation from the Milky Way may still have an appreciable effect at these source sizes for low galactic latitudes (e.g. Koopmans et al. 2003).

⁴ c.f., <http://www.vla.nrao.edu/astro/>

mass of any supermassive black hole that may reside at the center of the lens galaxy (Winn et al. 2003, 2004). Those constraints are based on radio data where, as noted above, the microlensing fluctuations are on the order of a few percent. However, even if they were as large as tens of percent, that would still be negligible compared with the orders of magnitude over which the macro magnifications of central images can vary due to modest changes in the smooth lens model (e.g., Keeton 2003). In other words, microlensing does not appear to be a significant concern for constraints on lens models drawn from radio observations of central images.

Perhaps even more interesting is the possibility that any central macro image produced by a lens galaxy containing a supermassive black hole should be accompanied by a second, fainter central image (Mao et al. 2001; Bowman et al. 2004), and that the central image pair can be used to measure the black hole mass quite precisely (Rusin et al. 2004). The second central image would be a saddle rather than a maximum, so it would be interesting to consider whether a central saddle would have different microlensing properties than the central maximum we have considered. We suspect that, at the radio wavelengths where this application would be pursued, microlensing fluctuations are still small compared with changes in the smooth lens model. Nevertheless, it would be interesting to understand in detail how microlensing of central saddles compares with microlensing of central maxima.

We are indebted to both anonymous referees for their helpful comments and suggestions. We thank David Rusin and Josh Winn for stimulating our interest in central images, and for providing results from lens models of PMN J1632–0033. We also thank Arthur Congdon for helpful discussions. GGD and CRK are supported by grant HST-AR-10668 from the Space Telescope Science Institute, which is operated by the Association of Universities for Research in Astronomy, Inc., under NASA contract NAS5-26555. JKW was supported by the European Community's Sixth Framework Marie Curie Research Training Network Programme, Contract No. MRTN-CT-2004-505183 "ANGLES".

REFERENCES

- Agol E., Krolik J., 1999, *ApJ*, 524, 49
- Bowman J. D., Hewitt J. N., Kiger J. R., 2004, *ApJ*, 617, 81
- Burke W. L., 1981, *ApJ*, 244, L1
- Chang K., Refsdal S., 1979, *Nature*, 282, 561
- Chang K., Refsdal S., 1984, *AA*, 132, 168
- Congdon A. B., Keeton C. R., Osmer, S. J., 2006, *MNRAS*, submitted
- Deguchi S., Watson W. D., 1987, *PRL*, 59, 2814
- Dyer C. C., Roeder R. C., 1980, *ApJ*, 238, L67
- Efron B., 1982, *The Jackknife, the Bootstrap, and Other Resampling Plans*. S.I.A.M., Philadelphia, PA
- Fluke C. J., Webster R. L., 1999, *MNRAS*, 302, 68
- Gaynullina E. R., et al., 2005, *AA*, 440, 53
- Goicoechea L. J., Shalyapin V., Gonaález-Cadela J., Oscoz A., 2004, *A&A*, 425, 475
- Gott J. R., 1981, *ApJ*, 243, 140
- Granot J., Schechter P. L., Wambsganss J., 2003, *ApJ*, 583, 575
- Grieger B., Kayser R., Refsdal S., 1988, *A&A*, 194, 54
- Grieger B., Kayser R., Schramm T., 1991, *A&A*, 252, 508
- Inada N., et al., 2005, *Publ.Astron.Soc.Jap.*, 57, L7
- Katz N., Balbus S., Paczynski B., 1986, *ApJ*, 306, 2
- Keeton C. R., 2003, *ApJ*, 582, 17
- Kochanek C. S., 2004, *ApJ*, 610, 69
- Kochanek C. S., et al., 2006, *ApJ*, 640, 47
- Koopmans L. V. E., de Bruyn A. G., 2000, *A&A*, 358, 793
- Koopmans L. V. E., et al., 2003, *ApJ*, 595, 712
- Lewis G. F., Ibata R. A., 2004, *MNRAS*, 348, 24
- Lewis G. F., Irwin M. J., 1995, *MNRAS*, 276, 103
- Mao S., Witt H. J., Koopmans L. V. E., 2001, *MNRAS*, 323, 301
- Mineshige S., Yonehara A., 1999, *PASJ*, 51, 497
- Morgan C. W., Kochanek C. S., Morgan N. D., Falco E. E., 2006, *ApJ*, 647, 874
- Mortonson M. J., Schechter P. L., Wambsganss J., 2005, *ApJ*, 628, 594
- Neindorf B., 2003, *AA*, 404, 83N
- Norbury M. A., Rusin D., Jackson N. J., Browne I. W. A., 2000, Abstracts from a conference held in Granada, 17-20 September 2000, and hosted by the Instituto de Radioastronomía Millimétrica (URAM), Universidad de Granada, and Instituto de Astrofísica de Andalucía (IAA)
- Paczynski B., 1986, *ApJ*, 301, 503
- Pelt J., Schild R., Refsdal S., Stabell R., 1998, *A&A*, 336, 829
- Petters A. O., Witt H. J., 1996, *Journal of Mathematical Physics*, 37, 2920
- Petters A. O., Levine H., Wambsganss J., 2001, *Singularity Theory and Gravitational Lensing*. Birkhäuser, Boston, MA
- Rauch K., Mao S., Wambsganss J., Paczyński B., 1992, *ApJ*, 386, 30
- Refsdal S., Stabell R., 1991, *A&A*, 250, 62
- Refsdal S., Stabell R., 1997, *A&A*, 325, 877
- Richards G. T., et al., 2004, *ApJ*, 610, 679
- Rusin D., Ma C.-P., 2001, *ApJ*, 549, L33
- Rusin D., Keeton C. R., Winn J. N., 2004, *ApJ*, 627, L93
- Schechter P. L., Udalski A., Szymański M., Kubiak M., Pietrzyński G., Soszyński I., Woźniak P., Żebruń K., Szweczyk O., Wyrzykowski L., 2003, *ApJ*, 584, 657
- Schechter P. L., Wambsganss J., 2002, *ApJ*, 580, 685
- Schechter P. L., Wambsganss J., 2004, in *IAU Symposium No. 220*, eds. S. D. Ryder, D. J. Pisano, M. A. Walker, and K. C. Freeman (San Francisco: Astronomical Society of the Pacific), p. 103
- Schechter P. L., Wambsganss J., Lewis G. F., 2004, *ApJ*, 613, 77
- Schmidt R., Wambsganss J., 1998, *A&A*, 335, 379
- Schneider P., 1987, *ApJ*, 319, 9
- Schneider P., Ehlers J., Falco E. E., 1992, *Gravitational Lenses*. Springer, Berlin
- Seitz C., Wambsganss J., Schneider P., 1994, *A&A*, 288, 1S
- Wallington S., Narayan R., 1993, *ApJ*, 403, 517
- Wambsganss J., PhD Thesis (Munich 1990), also MPA report 550
- Wambsganss J., Paczyński B., Katz N., 1990a, *ApJ*, 352, 407

- Wambsganss J., Paczyński B., Schneider P., 1990b, ApJ, 358, L33
- Wambsganss J., 1992, ApJ, 386, 19
- Wambsganss J., Witt H. J., Schneider P., 1992, A&A, 258, 591
- Wambsganss J., 1999, JCAM, 109, 353-372
- Winn J. N., Rusin D., Kochanek C. S., 2003, ApJ, 587, 80
- Winn J. N., Rusin D., Kochanek C. S., 2004, Nature, 427, 613
- Woźniak P. R., Alard C., Udalski A., Szymański M., Ku-
biak M., Pietrzyński G., Zebruń K., 2000, ApJ, 529, 88
- Wyithe J. S. B., Webster R. L., Turner E. L., 2000, MN-
RAS, 315, 51
- Wyithe J. S. B., Turner E. L., 2001, MNRAS, 320, 21
- Wyithe J. S. B., Turner E. L., 2002, ApJ, 575, 650